Definite existence of subphases with eight- and ten-layer unit cells as studied by complementary methods, electric-field-induced birefringence and microbeam resonant x-ray scattering

Zhengyu Feng,[1,2] A. D. L. Chandani Perera,[1,3] Atsuo Fukuda,[1] Jagdish K. Vij,[1] Ken Ishikawa,[2] Atsuo Iida,[4] and Yoichi Takanishi[5,*]

[1]*Department of Electronic and Electrical Engineering, Trinity College, University of Dublin, Dublin 2, Ireland*
[2]*Department of Organic and Polymeric Materials, Tokyo Institute of Technology, Meguro, Tokyo 152-8552, Japan*
[3]*Department of Chemistry, University of Peradeniya, Peradeniya 20400, Sri Lanka*
[4]*Photon Factory, Institute of Materials Structure Science, High Energy Accelerator Research Organization, 1-1 Oho Tsukuba, Ibaraki 305-0801, Japan*
[5]*Department of Physics, Faculty of Science, Kyoto University, Kitashirakawa-oiwake, Sakyou-ku, Kyoto 606-8502, Japan*

(Received 20 February 2017; revised manuscript received 30 March 2017; published 7 July 2017)

A mixture of two selenium-containing compounds, 80 wt. % AS657 and 20 wt. % AS620, are studied with two complementary methods, electric-field-induced birefringence (EFIB) and microbeam resonant x-ray scattering (μRXS). The mixture shows the typical phase sequence of Sm-C_A^*–$\frac{1}{3}$–$\frac{1}{2}$–Sm-C^*–Sm-C_α^*–Sm-A, where $\frac{1}{3}$ and $\frac{1}{2}$ are two prototypal ferrielectric and antiferroelectric subphases with three- and four-layer unit cells, respectively. Here we designate the subphase as its q_T number defined by the ratio of $[F]/([F]+[A])$, where $[F]$ and $[A]$ are the numbers of synclinic ferroelectric and anticlinic antiferroelectric orderings in the unit cell, respectively. The electric field vs temperature phase diagram with EFIB contours indicates the emergence of three additional subphases, an antiferroelectric one between Sm-C_A^* and $\frac{1}{3}$ and antiferroelectric and apparently ferrielectric ones between $\frac{1}{3}$ and $\frac{1}{2}$. The simplest probable q_T's for these additional subphases are $\frac{1}{4}$, $\frac{2}{5}$, and $\frac{3}{7}$, respectively, in the order of increasing temperature. The μRXS profiles indicate that antiferroelectric $\frac{1}{4}$ and $\frac{2}{5}$ approximately have the eight-layer ($FAAAFAAA$) and ten-layer ($FAFAAFAFAA$) Ising unit cells, respectively. The remaining subphase may be ferrielectric $\frac{3}{7}$ with a seven-layer unit cell, although the evidence is partial. These experimental results are compared with the phenomenological Landau model [P. V. Dolganov and E. I. Kats, Liq. Cryst. Rev. **1**, 127 (2014)] and the quasimolecular model [A. V. Emelyanenko and M. A. Osipov, Phys. Rev. E **68**, 051703 (2003)].

DOI: 10.1103/PhysRevE.96.012701

I. INTRODUCTION

A variety of optically biaxial polar subphases between the two main phases, anticlinic antiferroelectric Sm-C_A^* and synclinic ferroelectric Sm-C^*, was observed just after the discovery of Sm-C_A^* [1]. Electro-optical studies in the early stage already suggested that the two prototypal subphases have the unit cells of three-layer ferrielectric and four-layer antiferroelectric Ising structures, respectively. Furthermore, it was suggested that there exist some additional subphases with larger unit cells than three and four layers; the staircase emergence of these subphases as well as the prototypal ones can be appropriately specified by $q_T = [F]/([A]+[F])$, which constitutes the Farey sequence, where $[F]$ and $[A]$ are the numbers of synclinic ferroelectric and anticlinic antiferroelectric orderings in the unit cell, respectively [2–5]. Subphases with simpler q_T's tend to be actually observed more easily as their stability ranges would be wider. Meanwhile, an epoch-making finding was made by resonant x-ray scattering and optical studies: The biaxial subphases have nonplanar superlattice structures with microscopic highly distorted short-pitch helical director arrangements in their unit cells [6–12]. Since then it has been firmly established that the deviation from the Ising structures is not so large that $q_T = [F]/([A]+[F])$ is still useful to specify the subphases [13–21]; moreover, the microscopic short pitch of the highly distorted helix is given by $p_{qT} = 2/(1-q_T)$ in the unit of the number of smectic layers [19]. In what follows we designate the subphase just by specifying its q_T number like $\frac{1}{3}$, $\frac{1}{2}$, etc.

The frustration between the main phases, Sm-C_A^* and Sm-C^*, together with long-range interlayer interactions (LRILIs) has been considered to produce the subphases as a result of the temperature-induced sequence of phase transitions, as pointed out by Prost and Bruinsma [22,23]. It was not easy to find out LRILIs in polar smectics, where no truly positional order exists. Since LRILIs are weak, q_T increases monotonically with rising temperature. They proposed a type of Coulomb interaction resulting from the c-director (or polarization) fluctuations. This interaction is actually effective beyond next-to-nearest neighbors and a coupling between very distant layers is to be taken into account. The resulting model appears to be mathematically complex and no phase diagram was presented. Another effective LRILI between c-directors in distant layers was explored by Hamaneh and Taylor [24–26]. They included in the free energy of Sm-C^* the entropy due to thermal fluctuations in the shape of the smectic layers; they showed that the anisotropy in the bending elastic constant of a layer leads to a tendency for the c-directors in all layers to align in either a parallel or an antiparallel sense. The model actually explained the emergence of some subphases, but again no phase diagrams were given that can be compared with experimentally obtained ones including subphases with large unit cells.

Last but not least is an intriguing and useful effective LRILI devised by Emelyanenko and Osipov [27,28]. They introduced a fundamental concept of the discrete flexoelectric effect and wrote the free energy as the sum of the

*ytakanis@scphys.kyoto-u.ac.jp

polarization-independent part F_i and the polarization-dependent part ΔF_i. Here F_i is written phenomenologically by assuming the frustration between Sm-C_A^* and Sm-C^* on the basis of the constant large tilt angle; ΔF_i is derived from both phenomenological and molecular considerations and consists of the piezoelectric, flexoelectric, and polarization-polarization interaction terms. Although only the direct couplings between adjacent layers are reasonably taken into account, minimizing the free energy with respect to polarization brings about an effective LRILI that specifies director orientations in smectic layers within the unit cell of an arbitrary subphase. Thus we can determine numerically the highly distorted microscopic short-pitch helical structure of any subphase specified by q_T together with its stability range that can be compared with the experimentally obtained ones. Notice that we do not take into consideration chiral interactions between different layers, which must be very weak and are important only in the description of the macroscopic helical structure; nevertheless, the microscopic short-pitch helical structure inevitably emerges due to the molecular chirality.

In this way the quasimolecular model proposed by Emelyanenko and Osipov [27,28] is simple and straightforward and can be used to interpret experimental results. There is another theoretical approach to describe the sequential phase transitions in polar smectic liquid crystals that can also be compared with the experimental ones: The phenomenological Landau model reported by Dolganov *et al.* [29,30] is quite heuristic and automatically takes into account not only the temperature but also spatial changes of the tilt angle θ_i; it is not easy to perform minimization over the set of two-component order parameters, the azimuthal angle φ_i, and the tilt angle θ_i, although a variety of sequential emergence of subphases and the unit cell structures have already been given in their publications. Experimentally, in fact, the subphase emerging sequence is full of variety and the optically uniaxial polar Sm-C_α^* subphase may also emerge directly below Sm-A and replace Sm-C^* in some cases [19]. This is chiefly because another main phase Sm-A may participate in the frustration when the tilt angle becomes even closer to zero. The quasimolecular model proposed by Emelyanenko and Osipov can be expanded to include the frustration among the three main phases, as was actually carried out by Shtykov *et al.* [14]; in particular, the LRILI derived on the basis of the discrete flexoelectric effect has been modified to describe suitably the Sm-C_α^* free energy [19].

In this paper we take up the simplest case of the frustration between the main phases, Sm-C_A^* and Sm-C^*. Here the tilt angle can be considered to be large enough and almost constant (not only temperature-independent but also spatially uniform); furthermore, the main phases and the prototypal three- and four-layer subphases, $\frac{1}{3}$ and $\frac{1}{2}$, always emerge in the standard sequence of Sm-C_A^*–$\frac{1}{3}$–$\frac{1}{2}$–Sm-C^*. What is controversial is the existence of other subphases that may appear between Sm-C_A^* and Sm-C^* and have larger unit cells than those of $\frac{1}{3}$ and $\frac{1}{2}$. Some indirect evidence derived from electro-optical studies was reported that antiferroelectric $\frac{1}{4}$ and $\frac{2}{5}$ emerge between Sm-C_A^* and $\frac{1}{3}$ and between $\frac{1}{3}$ and $\frac{1}{2}$, respectively [19]. Takanishi *et al.* also confirmed ferrielectric six-layer $\frac{2}{3}$ between $\frac{1}{2}$ and Sm-C^* by microbeam resonant x-ray scattering (μRXS) in a slightly special compound that contains Br in the central part and has two chiral centers in the terminal chains [31].

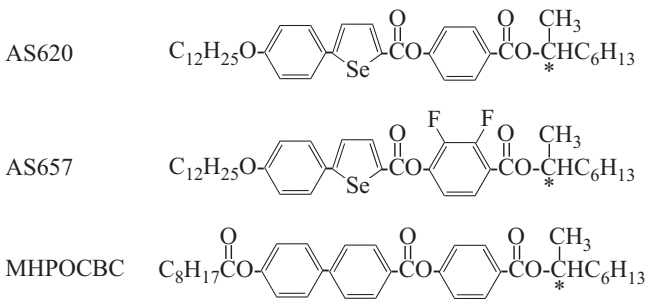

FIG. 1. Chemical formula of three compounds: AS620, AS657, and MHPOCBC. The *S* moieties were actually used.

Some researchers in the liquid-crystal field are, however, quite skeptical about the existence of subphases other than three-layer $\frac{1}{3}$, four-layer $\frac{1}{2}$, and six-layer $\frac{2}{3}$, particularly in the simplest standard emerging sequence [32]. They suspect the coexistence of the neighboring (sub)phases since the phase transitions are of first order. Therefore, we choose a Se-containing mixture that shows the standard emerging sequence and study it by measuring electric-field-induced birefringence (EFIB) and μRXS. These methods are complementary and are very effective to verify the emergence of subphases other than three-layer $\frac{1}{3}$, four-layer $\frac{1}{2}$, and six-layer $\frac{2}{3}$. As detailed in the following, we are sure that antiferroelectric eight-layer $\frac{1}{4}$ and ten-layer $\frac{2}{5}$ exist between Sm-C_A^* and $\frac{1}{3}$ and between $\frac{1}{3}$ and $\frac{1}{2}$, respectively. Moreover, an additional subphase may appear between $\frac{2}{5}$ and $\frac{1}{2}$, which can be identified as ferrielectric seven-layer $\frac{3}{7}$. These experimental results are compared with the phenomenological Landau model [29,30] and the quasimolecular model [27,28]. Some preliminary results of this paper have been reported at international conferences [33,34].

II. EXPERIMENT

A binary mixture of AS657 (80 wt. %) and AS620 (20 wt. %) was mainly used, which shows the standard sequential phase transitions indicating simple frustration between the main phases, Sm-C_A^* and Sm-C^*. We also used binary mixtures of AS657 and MHPOCBC as auxiliary samples. AS657 and AS620 are selenium containing compounds [35–37], which were purchased from Kingston Chemicals Ltd., University of Hull, Hull, UK, and MHPOCBC was synthesized by Showa Shell Sekiyu [38]. The chemical formula of these compounds are listed in Fig. 1.

Electric-field-induced birefringence was measured by using a photoelastic modulator (PEM-90, Hinds Instruments, Hillsboro, OR) with a resonant frequency of 50 kHz. Experimental details of measuring EFIB, birefringence Δn vs applied field E at various temperatures, were given in previous papers [14,15]. We followed the conventions that the electric field was applied along the y axis and that EFIB was defined as $\Delta n = n_x - n_y$ as in the previous papers. An improvement made in this study is the way of installing electrodes in

homeotropically (smectic layers parallel to substrate plates) aligned cells: Copper films of 37 μm thickness cut by a sharp knife are used as electrodes and spacers so that more uniform and higher fields are applied stably as compared to the previous indium tin oxide electrodes etched on a cell glass plate. The distance between the electrodes is adjusted to be around 200 μm, which is wider than the 25-mW He-Ne laser spot of about 80 μm in diameter used.

Microbeam resonant x-ray scattering experiments were performed on the 4A beamline at the Photon Factory (Japan) using homogeneously (smectic layers perpendicular to substrate plates) aligned cells. In order to investigate the local structure within uniform domains and at a particular temperature, we used an x-ray microbeam of a less than 5-μm^2 in cross section; the sample position can be adjusted within a precision of better than 1 μm. Experimental details were given in previous papers [31,39–41] and a brief summary is presented here for convenience. The sample was inserted into a 25-μm-thick sandwich cell whose substrates are 80-μm-thick glass plates coated with indium tin oxide as electrodes. By rubbing one of the substrates coated with polyimide (AL1254, JSR), uniformly planar domains were obtained. By applying a square wave electric field (20–1000 Hz, $\pm$3.8 V/μm) in antiferroelectric Sm-C_A^* and afterward heating up to the target temperatures after turning off the field, we could obtain quasibookshelf structures in the subphases. The sample cell was mounted on a compact heater, which had small windows (2 mm in diameter) for x-ray transmission. A platinum resistance thermometer sensor measured the temperature very close to this window. We particularly took care of the spatial gradient and the temporal stability of the sample temperature: About 0.1 °C/100 μm and $\pm$0.02 °C for more than one day were attained, when the hutch of the experimental cage was kept closed. A polarizing optical microscope with a CCD camera monitored the sample during the μRXS experiments. The major phase transition boundaries were usually clearly observed due in part to the spatial temperature gradient in the sample; the temperature calibration between different samples and several experimental runs was made by monitoring the major phase transition temperatures. The measurement was always carried out with increasing temperature.

The incident x-ray energy was set to the absorption edge of Se (12.65 keV). The layer normal was approximately horizontal and the incident beam was π polarized with respect to the reflection plane; hence the μRXS intensity in the present experiment was predominantly due to $\sigma\pi$ scattering (π incident and σ scattered x rays), since the μRXS theory predicts that the contribution from $\pi\pi$ scattering is negligibly weak [42]. A pixel array x-ray detector (Pilatus-100K, DECTRIS) was located at 85–100 cm from the sample. The exposure time for a two-dimensional (2D) diffraction pattern was typically about 30 min. Microbeam resonant x-ray scattering satellite peaks from the subphase at the resonant condition appear at

$$\frac{Q}{Q_0} = l + m[(1/\nu) \pm \epsilon], \tag{1}$$

where Q is the scattering vector, $Q_0 = 2\pi/d$, with d the smectic layer spacing, $l = \pm1, \pm2, \ldots$ is the diffraction order due to the fundamental periodicity d, ν is the number of layers in a subphase unit cell, $m = \pm1, \pm2, \ldots, \pm(\nu - 1)$ specifies satellite peak positions due to the superlattice periodicity νd, and $\epsilon = d/P$, with P the pitch of the macroscopic helix [6,8].

The first-order x-ray-diffraction intensity was measured as a function of the sample rotation angle (the ω-angular intensity profile) around the vertical axis to characterize the local layer structure. Then the Bragg condition was optimized for the satellite peak position of interest. The Q/Q_0 intensity distribution in the radial direction was extracted from the recorded 2D pattern. The first-order Bragg peak position in the 2D pattern was approximated as Q_0 and the obtained intensity distribution was analyzed semiquantitatively in terms of the Osipov-Gorkunov formula [42]. The intensity distribution from the cell structure sample was sensitive to the stability and perfection of the layer structure during the measurement. The μRXS reflections appearing near the forward scattering direction ($Q/Q_0 < 1$) were measured to attain reasonable detection efficiency, while a direct beam stopper blocked scattered x rays in the small-Q region. From geometrical conditions, the practical Q/Q_0 resolution of the measurement was about 0.005, although it depended on the counting statistics in practice.

III. RESULTS

A. Results of electric-field-induced birefringence

Figure 2 is the $E - T$ phase diagram of the mixture of AS657 (80 wt. %) and AS620 (20 wt. %) obtained in the heating process at a temperature step of 0.1°C. It also shows Δn at zero applied electric field at each temperature, which represents the cell alignment quality. Generally speaking, the quality is good and $\Delta n(E = 0)$ is well below 1×10^{-3} when the helical pitch is short; in the subphase temperature regions, however, it may become as large as $\sim 3 \times 10^{-3}$ since subphases usually have longer macroscopic helical pitches than the main phases Sm-C_A^* and Sm-C^*. The corresponding cooling data obtained just before the heating measurements lead to an $E - T$ phase diagram rather similar to Fig. 2; thermal hysteresis is not prominent. The prototypal subphases, $\frac{1}{3}$, $\frac{1}{2}$, and Sm-C_α^*, as well as the main phases, Sm-C_A^* and Sm-C^*, can be seen as indicated in Fig. 2. To see the details of the phase transition regions, we performed 0.02 °C–step measurements in the cooling and heating processes and the resulting $E - T$ phase diagram is illustrated in Fig. 3.

Let us begin with the temperature range between Sm-C_A^* and $\frac{1}{3}$. On taking a closer look at Fig. 3, we could not make it clear whether or not there exists another subphase. In fact, when we look at the $\Delta n - E$ curves at a larger temperature step, we can only see the main antiferroelectric phase Sm-C_A^* and the ferrielectric subphase $\frac{1}{3}$ in the low- and high-temperature ranges as in Fig. 4. One may ask why Sm-C_A^* does not show any negative EFIB Δn at these temperatures; at much lower temperatures negative Δn is clearly observed and in fact, even at 85.20 °C, Δn becomes slightly negative just before the steep rise, as can be seen in Fig. 4. The reason lies in the helical structure of Sm-C_A^* and in the two mechanisms of producing net spontaneous polarization. When the antiferroelectric phase is stable enough, an applied field induces net spontaneous polarization so that the average tilting directions orient parallel to the field [43–48]. When

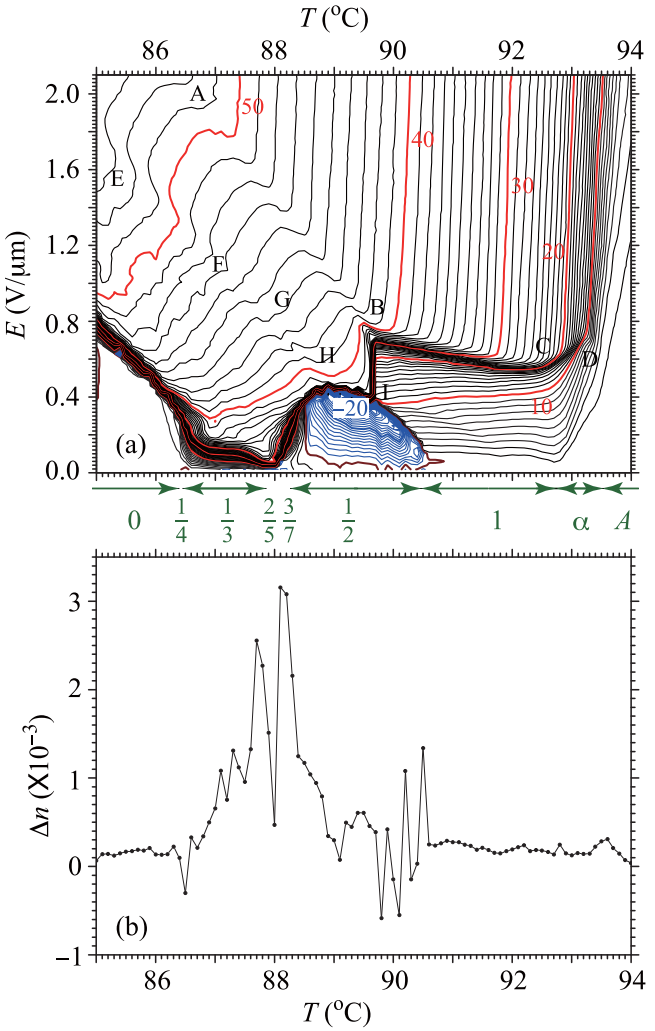

FIG. 2. (a) The $E-T$ phase diagram with EFIB Δn contours and (b) $\Delta n - T$ at zero applied electric field in the mixture of AS657 (80 wt. %) and AS620 (20 wt. %) obtained in the heating process with a 37-μm-thick homeotropically (smectic layers parallel to substrate plates) aligned cell. A very similar phase diagram was obtained in the cooling process. The temperature step was 0.1 °C and the electric-field step was 0.021 V/μm; the electrode gap was 200 μm. Contours are plotted at a step of 1×10^{-3}. The temperature ranges of the subphases and the main phases are indicated by their q_T numbers between (a) and (b); α and A represent Sm-C^*_α and Sm-A, respectively. The emergence of subphases $\frac{1}{4}$, $\frac{2}{5}$, and $\frac{3}{7}$ is to be confirmed in this paper.

it is not so stable as in the peripheral region near the phase transition temperature, an applied field changes some of its unit cells into ferroelectric or ferrielectric, produces additional net spontaneous polarization, and tends to align the average tilting directions perpendicular to the field [49]. Unwinding of the helical structure and the resulting alignment may occur parallel or perpendicular to the field and hence show negative or positive Δn depending on which net spontaneous polarization becomes predominant.

Now we examine $\Delta n - E$ curves plotted at a step of 0.02 °C shown in Fig. 5. The curve seems to change gradually from Sm-C^*_A to $\frac{1}{3}$ in Fig. 5(a) obtained in the cooling process, indicating the mere coexistence of the two adjacent phases

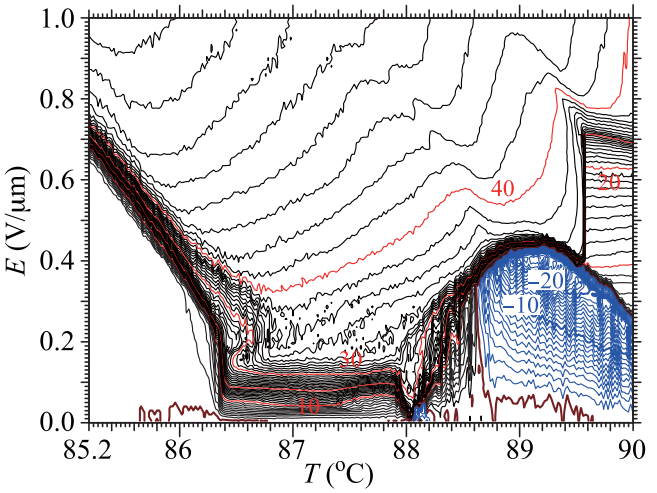

FIG. 3. The $E-T$ phase diagram of the AS657 (80 wt. %)–AS620 (20 wt. %) mixture measured in the heating process with the same cell as used in Fig. 2. The temperature step was 0.02 °C and the electric-field step was 0.01 V/μm. A very similar phase diagram was obtained in the cooling process.

because of the first-order phase transition. In Fig. 5(b), obtained in the heating process, however, two $\Delta n - E$ curves at 86.32 °C and 86.34 °C almost overlap each other. The overlapping could hardly be explained by the mere coexistence of Sm-C^*_A and $\frac{1}{3}$ and indicates the existence of an additional subphase between them, the stability range of which is as narrow as about 0.04 °C. The reason why the overlapping is not observed in the cooling process is that there exists thermal hysteresis on the same level with the stability range of the additional subphase, at about 0.02 °C. When we take a closer look at Fig. 5(a), in fact, we notice that the $\Delta n - E$ curve at 86.32 °C is rather isolated; this suggests the emergence of an additional subphase with the stability rage as narrow as the

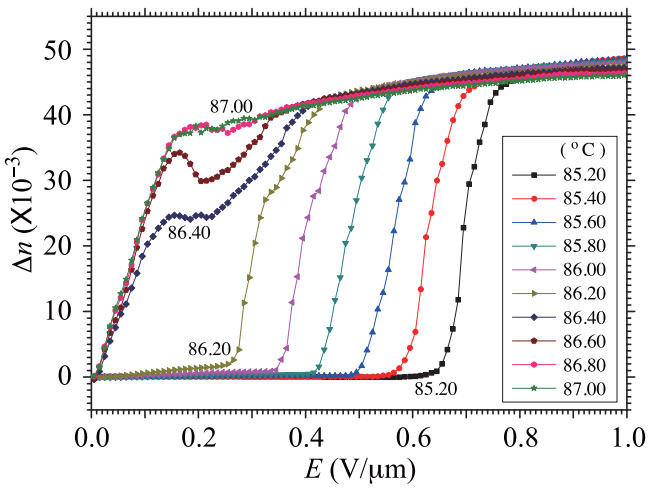

FIG. 4. The $\Delta n - E$ curves plotted at a step of 0.2 °C near the temperature range between Sm-C^*_A and $\frac{1}{3}$ for the heating process. The phase transition from Sm-C^*_A to $\frac{1}{3}$ appears to occur directly between 86.20 °C and 86.40 °C at this temperature step. The threshold exists in antiferroelectric Sm-C^*_A but not in ferrielectric $\frac{1}{3}$.

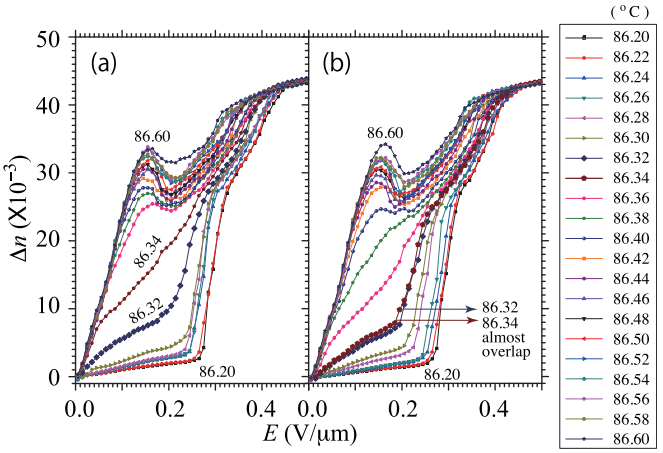

FIG. 5. Original data of $\Delta n - E$ curves measured at a step of 0.02 °C near the temperature range between Sm-C_A^* and $\frac{1}{3}$ in the (a) cooling and (b) heating processes. At this temperature step we can anticipate the emergence of an additional subphase between Sm-C_A^* and $\frac{1}{3}$. For further details see the text.

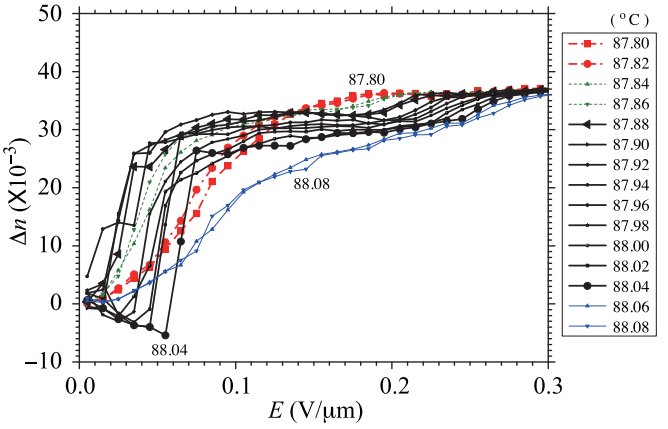

FIG. 6. The $\Delta n - E$ curves observed at a temperature step of 0.02 °C in the cooling process. The $\Delta n - E$ curves drawn by thick solid lines between 87.88 °C and 88.04 °C rise very steeply and becomes negative in the lower temperature part, suggesting the emergence of an additional antiferroelectric subphase. See the text for further details.

temperature changing step even in the cooling process. Thus we are now convinced that an additional subphase emerges between Sm-C_A^* and $\frac{1}{3}$, the stability range of which is as narrow as about 0.02 °C–0.04 °C. The additional subphase must have $q_T = \frac{1}{4}$ and a unit cell consisting of at least eight layers, since the simplest Farey sequence number between 0 and $\frac{1}{3}$ is $\frac{1}{4}$ and the $(FAAA)$ sequence could not be realized in the four-layer unit cell. Furthermore, since the $\Delta n - E$ curves at 86.32 °C–86.34 °C suggesting the emergence of $\frac{1}{4}$ in Fig. 5 show a rather steep thresholdlike increase, the anticipated subphase must be antiferroelectric. In Sec. III B we confirm by μRXS that the additional subphase is eight-layer $\frac{1}{4}$.

Let us proceed to the temperature range between $\frac{1}{3}$ and $\frac{1}{2}$. Here, just taking a cursory look at Fig. 3 is enough to believe the emergence of at least another subphase, because the existence of the valley with some negative contours at around 88 °C cannot be explained by the mere coexistence of $\frac{1}{3}$ and $\frac{1}{2}$; both Δn's are positive on the high-temperature side of $\frac{1}{3}$ and on the low-temperature side of $\frac{1}{2}$. If there were to be their coexistence, we would have positive contours. The emergence becomes much clearer in $\Delta n - E$ curves plotted at a 0.02 °C step shown in Fig. 6. In the temperature range of 0.16 °C between 87.88 °C and 88.04 °C, the $\Delta n - E$ curve rises very steeply and in particular it becomes unambiguously negative between 87.96 °C and 88.04 °C; the negative values are of the order of $\Delta n \sim -10^{-3}$, one order of magnitude larger than that of the background noise level shown in Fig. 2(b). Thus we secure the emergence of an additional antiferroelectric subphase between $\frac{1}{3}$ and $\frac{1}{2}$. Its stability range is about 0.16 °C or slightly larger as the $\Delta n - E$ curve at 87.84°C as well as 87.86 °C may also belong to the subphase. The change from $\frac{1}{3}$ on the low-temperature side is rather continuous and their coexistence temperature range must be rather narrow. On the high-temperature side, contrastingly, the negative EFIB suddenly disappears between 88.04 °C and 88.06 °C, as can be seen in Fig. 6. In Sec. III B this additional antiferroelectric subphase is identified as ten-layer $\frac{2}{5}$ by μRXS.

Now we move on to the temperature range between $\frac{2}{5}$ and $\frac{1}{2}$, where it is quite noisy, as can be seen in Fig. 3. Here again we take a close look at the original data, the $\Delta n - E$ curves obtained at a step of 0.02 °C and reproduced in Fig. 7. The $\frac{2}{5}$ boundary on the high-temperature side is clear, as pointed out above, but the $\frac{1}{2}$ boundary on the low-temperature side is vague since its lower-temperature part, like the higher-temperature part of Sm-C_A^*, shows positive Δn in an applied electric field. We tentatively assume that 88.46 °C is the $\frac{1}{2}$ boundary below which the threshold seems to disappear. Then it is

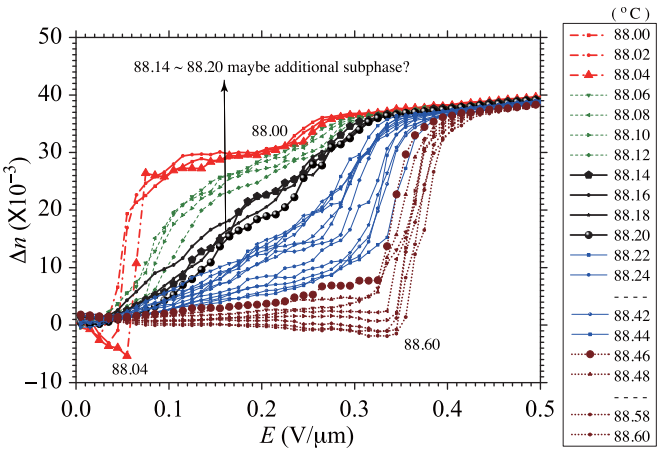

FIG. 7. The Δn-E curves observed at a temperature step of 0.02 °C in the cooling process. The Δn-E curves that apparently appear between $\frac{2}{5}$ and $\frac{1}{2}$ were tentatively divided into three groups: the curves drawn by thick solid black lines in the middle temperatures of 88.14 °C–88.20 °C represents an additionally emerging subphase and the thin dotted green curves at 88.06 °C–88.12 °C and the thin solid blue curves at 88.22 °C–88.44 °C represent the adjacent coexistence ranges on the low- and high-temperature sides, respectively. The thick dash-dotted red curves and the thick dotted brown curves represent $\frac{2}{5}$ and $\frac{1}{2}$ subphases, respectively. See the text for further details.

not impertinent to consider that there exists a middle range (88.14 °C–88.20 °C) representing a subphase with adjacent coexistence ranges (88.06 °C–88.12°C and 88.22 °C–88.44°C). The simplest possible candidate for this additional subphase is a ferrielectric seven-layer $\frac{3}{7}$ subphase [27,50], although we have not been able to confirm its emergence clearly by μRXS yet as will be explained in Sec. III B.

Before closing this section, let us make a brief survey of electric-field-induced subphases. To begin with, we take up the inverted sigmoid curves of contours observed around 86.6 °C and 0.2 V/μm in the $E-T$ phase diagram of Fig. 3; these appear in the lower-temperature range of $\frac{1}{3}$. When we looked at these from another perspective and follow Δn at a fixed temperature with increasing applied field as shown in Figs. 4 and 5, Δn first rises steeply without any threshold, showing a peak near 0.15–0.17 V/μm, decreases slightly to attain a valley near 0.19–0.21 V/μm, and then increases again. The steep rise simply indicates the field-induced unwinding of the macroscopic long-pitch helix of the temperature-induced $\frac{1}{3}$ subphase. Around the peak, when it is high enough, the almost unwound $\frac{1}{3}$ subphase is considered to be realized; hence the decrease and the subsequent emergence of a valley unambiguously indicate that another field-induced subphase is stabilized around there, the unit cell of which must be larger than the three-layer of $\frac{1}{3}$ and has a larger deviation from the planar structure due to the microscopic short-pitch distorted helix [49]. We speculate that it may be a five-layer $q_E = \frac{3}{5}$, which consists of a three-layer ferrielectric (RRL) and a two-layer ferroelectric (RR) that is field-induced from a two-layer antiferroelectric (RL). Here R and L refer to the smectic layer with directors tilted to the right and left, respectively.

Aside from the fairly specific field-induced subphase explained above, here we look at the bigger picture of the $E-T$ phase diagrams illustrated in Figs. 2 and 3. When the applied field becomes high enough, the completely unwound Sm-C^* phase is realized and the contour curves become almost vertical, i.e., parallel to the ordinate axis. The shape of contours just before the field-induced transition to unwound Sm-C^* looks quite different in the low- and high-temperature ranges. The macroscopic long-pitch helix of Sm-C^* and the microscopic short-pitch helix of Sm-C^*_α are simply unwinding at temperatures higher than ~89.6 °C. At lower temperatures, on the other hand, some transitions seem to occur from field-induced subphases to unwound Sm-C^* near the line connecting A and B in Fig. 2; furthermore, nearly 0.2–0.5 V/μm below unwound Sm-C^* some other transitions occur between field-induced subphases near the line connecting E, F, G, and H in Fig. 2. These transitions can be seen as steep increases along the lines AB and GH and minima along the line EF in the $\Delta n - E$ diagram as illustrated in Fig. 8. In particular, the minima along the line EF correspond to the sigmoid-shaped contours in Fig. 2 at temperatures lower than ~87.2 °C. This means that the unit cell of the higher-field subphase contains more smectic layers and has a larger deviation from the planar structure due to the microscopic short-pitch distorted helix as compared to the unit cell of the lower-field subphase [49]. No μRXS study has been made by applying an electric field in this particular mixture yet. It would clarify many intriguing aspects about field-induced subphases, as the previous investigations were not performed by using these complementary methods [40,41].

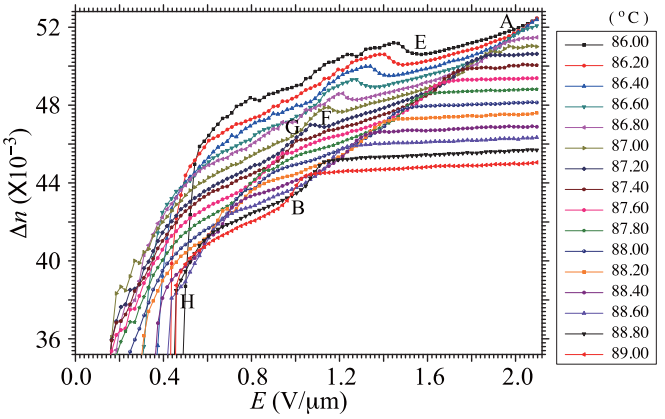

FIG. 8. The $\Delta n - T$ curves at a temperature step of 0.2 °C obtained by plotting the original data used in drawing Fig. 2. Here lines AB, EF, and GH correspond to those in Fig. 2 and represent some field-induced transitions. See the text for further details.

B. Results of microbeam resonant x-ray scattering

Microbeam resonant x-ray scattering data near the phase transition boundary between Sm-C^*_A and $\frac{1}{3}$ are shown in Figs. 9 and 10. The boundary is usually clearly observed *in situ* by the installed polarizing optical microscope with the CCD camera. The temporal fluctuation of the oven is better than ±0.02 °C during the experiments. The spatial temperature gradient in the

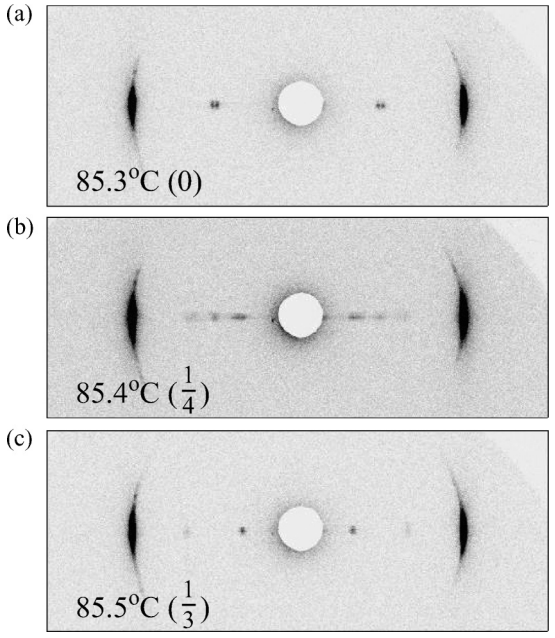

FIG. 9. The μRXS 2D patterns of the mixture of AS657 (80 wt. %) and AS620 (20 wt. %) at (a) 85.3 °C, (b) 85.4 °C, and (c) 85.5 °C.

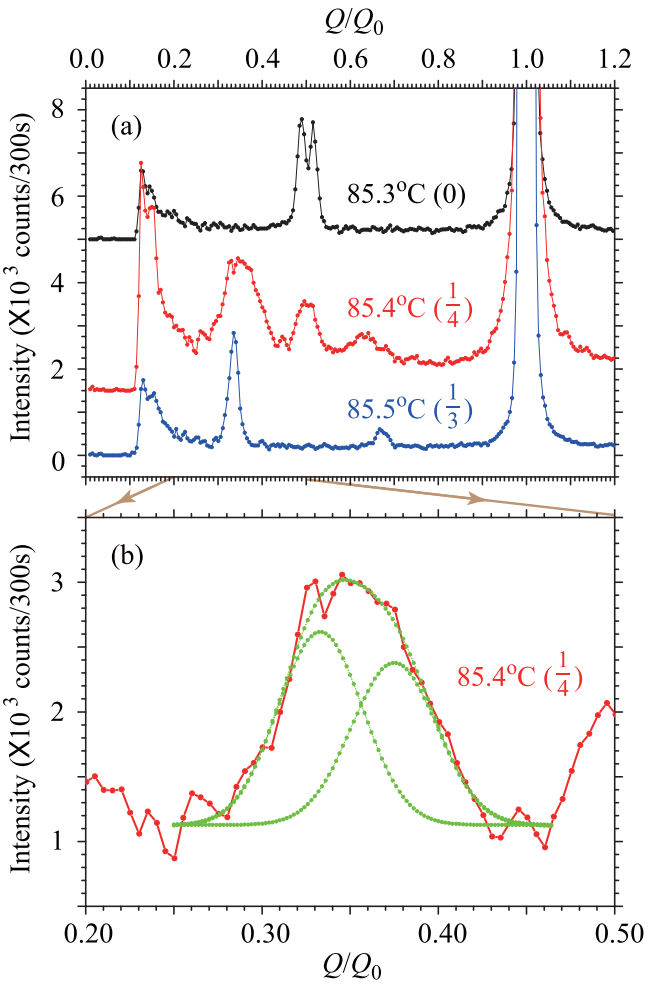

FIG. 10. The μRXS intensity profiles along the layer normal as a function of the normalized scattering vector (Q/Q_0, where $Q_0 = 2\pi/d$ and d is a layer spacing) in two-layer Sm-C_A^* at 85.3 °C, eight-layer $\frac{1}{4}$ at 85.4 °C, and three-layer $\frac{1}{3}$ at 85.5 °C of the mixture of AS657 (80 wt. %) and AS620 (20 wt. %), which were extracted from Fig. 9. At 85.4 °C it was hard to separately observe the 3/8-order peak of eight-layer $\frac{1}{4}$ and the 1/3-order peak of three-layer $\frac{1}{3}$, but the composite peak is successfully decomposed into the two peaks as illustrated in (b).

sample is about 0.1 °C/100 μm, whereas the monochromatic x-ray beam size is less than 5 μm^2 in cross section. The irradiated point can be adjusted within an accuracy of better than ± 1 μm. Hence we can expect to detect the eight-layer $\frac{1}{4}$ subphase with the temperature stability range as narrow as 0.02 °C–0.04 °C, which was predicted to emerge by EFIB as shown in Fig. 5. In fact, we performed μRXS near the boundary and successfully obtained the 2D patterns illustrated in Fig. 9. Then we extracted the μRXS profiles along the radial direction as shown in Fig. 10, where the temperatures indicated are the nominal ones measured by the platinum resistance thermometer.

The profile at 85.3 °C with a 1/2-order peak and the profile at 85.5 °C with 1/3- and 2/3-order peaks represent antiferroelectric Sm-C_A^* and ferrielectric $\frac{1}{3}$, respectively. The splitting of the 1/2-order peak is due to the macroscopic

TABLE I. Four conceivable eight-layer $\frac{1}{4}$ Ising unit cells and the squares of the corresponding relative structure factor for each peak. Since $n/8$ and $(8-n)/8$ peaks are of the same value, only $n = 1,2,\ldots,4$ are listed. Actually observed intensity profiles shown in Fig. 10 were obtained under the Bragg condition optimized to a particular satellite peak position of interest; no geometrical corrections were made for measured x-ray intensity.

No.	q_T	Unit cell	State	(structure factor)^2
1	$\frac{1}{4}$	$(FFAAAAAA)$	ferrielectric	4.0, 4.0, 4.0, 36.0
2		$(FAFAAAAA)$	antiferroelectric	2.3, 8.0, 13.7, 16.0
3		$(FAAFAAAA)$	ferrielectric	0.7, 4.0, 23.3, 4.0
4		$(FAAAFAAA)$	antiferroelectric	4.7, 0.0, 27.3, 0.0

helical structure of Sm-C_A^* with a pitch of about 0.25 μm, i.e., $\epsilon = 0.014$ in Eq. (1). The profile at 85.4 °C in between could not be reproduced by overlapping of the 1/2-, 1/3-, and 2/3-order peaks due to a mere coexistence of neighboring Sm-C_A^* and $\frac{1}{3}$; it clearly indicates the emergence of some additional subphase(s) with unit cells that prominently produce satellite diffraction peaks at around $Q/Q_0 = 0.35$–0.4 and 0.6–0.65. Unfortunately, the newly appearing peaks are broad and the temperature is not sufficiently stable temporally, so the overlapping of the 1/3- and 2/3-order peaks of the three-layer $\frac{1}{3}$ subphase could not be avoided completely. Therefore, it is hard to determine the newly appearing satellite peak positions precisely.

Here we examine to what extent the observed profile at 85.4 °C can be explained by assuming the emergence of an eight-layer $\frac{1}{4}$ subphase; notice that the simplest Farey sequence number between 0 and $\frac{1}{3}$ is $\frac{1}{4}$ and an eight-layer unit cell is the smallest one since the $(FAAA)$ sequence could not be realized in a four-layer unit cell. Table I summarizes the whole conceivable eight-layer $\frac{1}{4}$ Ising unit cells with the μRXS satellite relative intensities calculated using the Osipov-Gorkunov formula [42]. Among these four unit cells, only two have prominently strong 3/8- and 5/8-order peaks as illustrated in Fig. 11. Since the anticipated subphase must be antiferroelectric as pointed out in regard to Fig. 5, it is not impertinent to conclude that the anticipated subphase has approximately the Ising structure of No. 4 in Table I. In fact, the observed profile at 85.4 °C can be reproduced by overlapping 3/8- and 1/3-order peaks as shown in Fig. 10(b). The

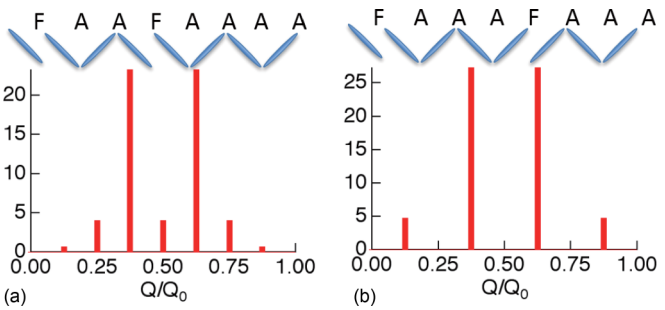

FIG. 11. Two unit cells and their μRXS intensity profiles, i.e., Nos. 3 and 4 in Table I, that have prominently strong 3/8- and 5/8-order peaks.

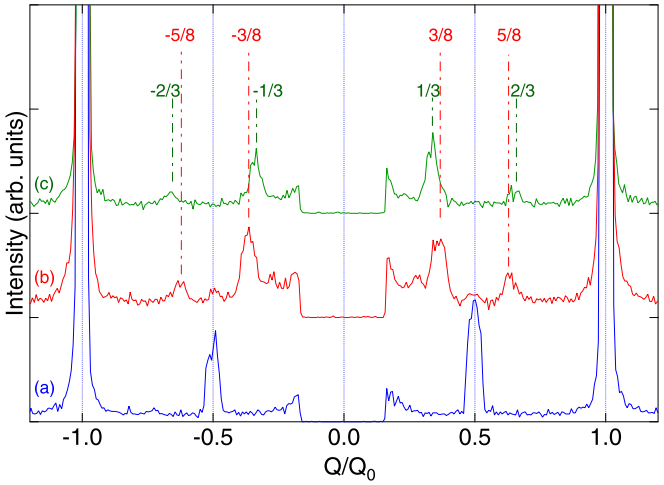

FIG. 12. The μRXS intensity profiles corresponding to Fig. 10 in a different mixture of AS657 (90 wt. %) and MHPOCBC (10 wt. %) for two-layer Sm-C_A^* at (a) 86.5 °C, eight-layer $\frac{1}{4}$ at (b) 86.7 °C, and three-layer $\frac{1}{3}$ at (c) 87.0 °C.

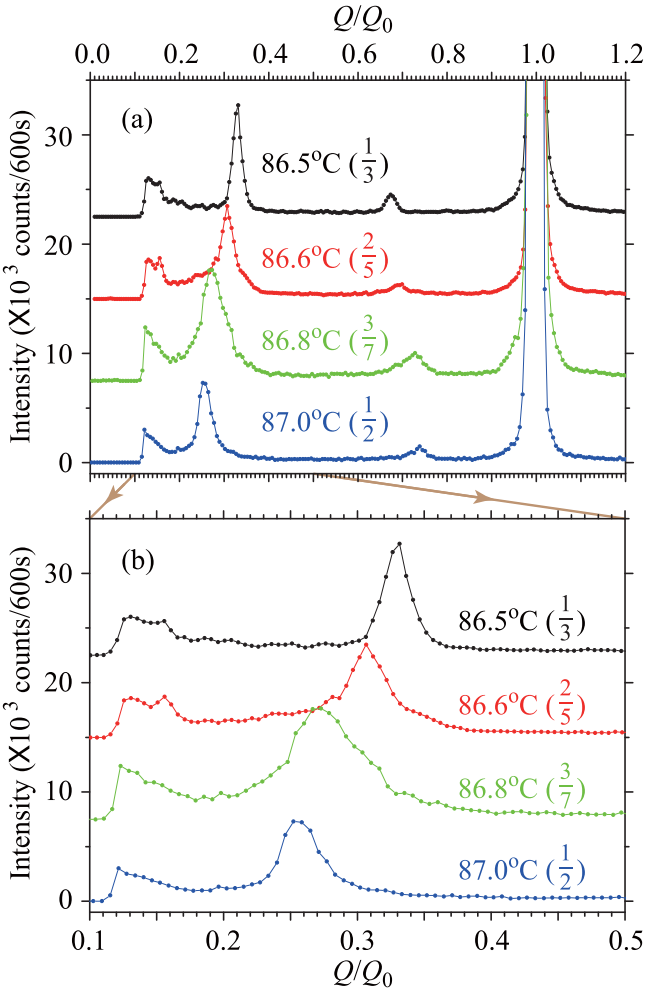

FIG. 13. The μRXS intensity profiles along the layer normal as a function of the normalized scattering vector (Q/Q_0, where $Q_0 = 2\pi/d$ and d is a layer spacing) in three-layer $\frac{1}{3}$ at 86.5 °C, ten-layer $\frac{2}{5}$ at 86.6 °C, and four-layer $\frac{1}{2}$ at 87.0 °C of the mixture of AS657 (80 wt. %) and AS620 (20 wt. %). An additional subphase appears to emerge at around 86.8 °C, but it is hard to identify as seven-layer $\frac{3}{7}$ uniquely. See the text for further details.

emergence of the 1/2-order peak may represent a departure from the flat Ising structure, i.e., a highly distorted helical structure with a microscopic short pitch of three turns per eight layers ($p_{qT} = 8/3$); it may also due to the coexistence of Sm-C_A^* though. The broadness of the 3/8- and 5/8-order peaks may be due to the unresolved peak splitting caused by the macroscopic helical structure of the eight-layer subphase and/or the rather short coherence length of the eight-layer structure resulting from the temperature stability range as narrow as 0.02 °C–0.04 °C. The somewhat narrower 3/8- and 5/8-order peaks were observed in a different mixture of AS657 (90%) and MHPOCBC (10%), as shown in Fig. 12, although no detailed investigations have been made yet.

Electric-field-induced birefringence data summarized in Figs. 3 and 6 unambiguously show the emergence of an additional antiferroelectric subphase between $\frac{1}{3}$ and $\frac{1}{2}$. This additional subphase must have $q_T = \frac{2}{5}$, for the simplest Farey sequence number between $\frac{1}{3}$ and $\frac{1}{2}$ is $\frac{2}{5}$, which has a unit cell as large as at least ten-layer periodicity; notice that sequences such as $(FFAAA)$ and $(FAFAA)$ with apparent periodicity could not be realized in the five-layer unit cell. In fact, the μRXS data shown in Fig. 13 unequivocally indicate that the subphase has a ten-layer unit cell; the newly appearing satellite diffraction peaks are observed at $Q/Q_0 = 0.300 \pm 0.005$ and 0.700 ± 0.005. We now consider the director arrangement of the ten-layer $\frac{2}{5}$ subphase. Table II summarizes the whole conceivable ten-layer $\frac{2}{5}$ Ising unit cell with the μRXS satellite relative intensities calculated using the Osipov-Gorkunov formula [42]; only six of them are antiferroelectric and the remaining ten are ferrielectric. Taking a look at Fig. 13 again, we immediately notice that the 3/10 and 7/10 satellite peaks are prominently strong. Table II indicates that Nos. 15 and 16 unit cells actually give such satellite patterns. Since this ten-layer $\frac{2}{5}$ subphase is antiferroelectric as pointed out with regard to Fig. 6, we can reasonably conclude that it should be the No. 16 unit cell in the Ising model approximation. Even when we consider all the 39 ten-layer Ising unit cells, four with $q_T = \frac{1}{5}$, sixteen with $\frac{2}{5}$, fourteen with $\frac{3}{5}$, and five with $\frac{4}{5}$, we arrive at the same conclusion inevitably.

The original Δn-E curves measured at a temperature step of 0.02 °C shown in Fig. 7 appear to indicate the emergence of a ferrielectric seven-layer $\frac{3}{7}$ subphase. Figure 13 also illustrates μRXS intensity profiles at 86.8 °C. An additional peak appears to emerge at around $Q/Q_0 = 2/7 = 0.286$ between $\frac{2}{5}$ at 86.6 °C and $\frac{1}{2}$ at 87.0 °C, but at the same time there exists considerable overlapping of the $\frac{2}{5}$ and $\frac{1}{2}$ peaks at $Q/Q_0 = 3/10 = 0.3$ and $1/4 = 0.25$, respectively. The three peaks overlapping makes it difficult to determine the additional peak position accurately. Suppose the additional peak is due to $\frac{3}{7}$; again the approximate Ising unit cell is uniquely determined as No. 4 given in Table III, although the evidence for the emergence of the ferrielectric seven-layer $\frac{3}{7}$ subphase is partial. We would like to perform more elaborate investigations in the near future.

TABLE II. Sixteen conceivable ten-layer $\frac{2}{5}$ Ising unit cells and the squares of the corresponding relative structure factor for peaks $n = 1,2,\ldots,5$. Actually observed intensity profiles shown in Fig. 13 were obtained under the Bragg condition optimized to a particular satellite peak position of interest; no geometrical corrections were made for measured x-ray intensity.

No.	Unit cell	State	(structure factor)^2
1	$(FFFFAAAAAA)$	ferrielectric	10.5, 1.5, 1.5, 10.5, 36.0
2	$(FFFAFAAAAA)$	ferrielectric	10.5, 9.5, 1.5, 18.5, 16.0
3	$(FFFAAFAAAA)$	ferrielectric	4.0, 7.1, 4.0, 24.9, 4.0
4	$(FFFAAAFAAA)$	ferrielectric	14.5, 0.6, 5.5, 27.4, 0.0
5	$(FFAFFAAAAA)$	antiferroelectric	10.5, 14.5, 1.5, 5.5, 36.0
6	$(FFAAFFAAAA)$	ferrielectric	1.5, 10.5, 10.5, 1.5, 36.0
7	$(FFAAAFFAAA)$	antiferroelectric	16.0, 0.0, 16.0, 0.0, 36.0
8	$(FFAFAFAAAA)$	ferrielectric	1.5, 18.5, 10.5, 9.5, 16.0
9	$(FFAFAAFAAA)$	antiferroelectric	9.5, 5.5, 18.5, 14.5, 4.0
10	$(FFAFAAAFAA)$	ferrielectric	5.5, 9.5, 14.5, 18.5, 0.0
11	$(FFAFAAAAFA)$	antiferroelectric	4.0, 20.0, 4.0, 20.0, 4.0
12	$(FFAAFAFAAA)$	ferrielectric	7.1, 4.0, 24.9, 4.0, 16.0
13	$(FFAAFAAFAA)$	ferrielectric	0.6, 1.5, 27.4, 10.5, 4.0
14	$(FAFAFAFAAA)$	antiferroelectric	0.6, 14.5, 27.4, 5.5, 4.0
15	$(FAFAFAAFAA)$	ferrielectric	2.1, 4.0, 37.9, 4.0, 0.0
16	$(FAFAAFAFAA)$	antiferroelectric	6.1, 0.0, 41.9, 0.0, 4.0

IV. DISCUSSION

The EFIB studies clarify the emergence of two antiferroelectric subphases between Sm-C_A^* and $\frac{1}{3}$ and between $\frac{1}{3}$ and $\frac{1}{2}$, respectively. The simplest probable q_T's for these additional subphases are $\frac{1}{4}$ and $\frac{2}{5}$ in the order of increasing temperature. The studies also allude to the emergence of an additional ferrielectric subphase with the simplest probable q_T of $\frac{3}{7}$ between $\frac{2}{5}$ and $\frac{1}{2}$. In fact, the μRXS studies indicate that the antiferroelectric subphase between Sm-C_A^* and $\frac{1}{3}$ has an eight-layer unit cell and that the antiferroelectric subphase between $\frac{1}{3}$ and $\frac{1}{2}$ has a ten-layer unit cell. The remaining additional subphase between $\frac{2}{5}$ and $\frac{1}{2}$ is considered to have a seven-layer unit cell, although the evidence is partial. Thus we have the phase emerging sequence: Sm-C_A^*–$\frac{1}{4}$–$\frac{1}{3}$–$\frac{2}{5}$–($\frac{3}{7}$)–$\frac{1}{2}$–Sm-C^*. Moreover, the μRXS studies specify the most probable Ising unit cells for $\frac{1}{4}$, $\frac{2}{5}$, and $\frac{3}{7}$ as given in Tables I–III, respectively. In particular, the existence of antiferroelectric ten-layer $\frac{2}{5}$ that has approximately the Ising $(FAFAAFAFAA)$ unit cell is unequivocally ensured by the complementary studies of EFIB and μRXS. Now let us compare the current and some of the previous experimental results with the theoretical predictions by the phenomenological Landau model [29,30] and the quasimolecular model [27,28].

TABLE III. Four conceivable seven-layer $\frac{3}{7}$ Ising unit cells and the squares of the corresponding relative structure factor for peaks $n = 1$, 2, and 3. See Table II caption also.

No.	Unit cell	State	(structure factor)^2		
1	$(FFFAAAA)$	ferrielectric	6.2	0.8	13.0
2	$(FFAAFAA)$	ferrielectric	0.8	13.0	6.2
3	$(FFAAAFA)$	ferrielectric	8.0	8.0	8.0
4	$(FAAFAFA)$	ferrielectric	2.6	20.2	1.2

We begin with the antiferroelectric $\frac{1}{4}$ subphase that has approximately the eight-layer Ising $(FAAAFAAA)$ unit cell. The emergence of antiferroelectric $\frac{1}{4}$ just above Sm-C_A^* has been experimentally suggested since Chandani *et al.* studied the Bragg reflection and optical rotatory power due to the macroscopic helical director arrangements together with EFIB in the mixtures of (*S*)-12BIMF10 and (*S*)-MHPBC [15]. The beautiful (green and red) Bragg reflection texture they observed could not be explained by the mere coexistence of the adjacent (sub)phases and clearly indicates the emergence of an additional subphase. They considered that the observed additional subphase must have $q_T = \frac{1}{4}$, as this is the simplest Farey sequence number less than $\frac{1}{3}$. Sandhya *et al.* also suggested the appearance of $\frac{1}{4}$ just above Sm-C_A^* in the global evolution of phase emerging sequence in the mixture system of MHPOCBC and MHPOOCBC [20]:

(1) Sm-C_A^*–Sm-C_α^*–Sm-A,

(2) Sm-C_A^*–$\frac{1}{3}$–Sm-C_α^*–Sm-A,

(3) Sm-C_A^*–$\frac{1}{3}$–$\frac{1}{2}$–Sm-C_α^*–Sm-A,

(4) Sm-C_A^*–$\frac{1}{3}$–$\frac{1}{2}$–Sm-C^*–Sm-C_α^*–Sm-A,

(5) Sm-C_A^*–$\frac{1}{3}$–Sm-C^*–Sm-C_α^*–Sm-A,

(6) Sm-C_A^*–Sm-C^*–Sm-C_α^*–Sm-A.

Their results indicate that the stability range of $\frac{1}{4}$ is more than 0.2 °C in sequence (2) and that in particular it may appear between Sm-C_A^* and Sm-C_α^* in sequence (1). The current experiments are performed in sequence (4) and the stability range of $\frac{1}{4}$ is about 0.02 °C; still we were able to determine the approximate Ising unit cell structure by using both EFIB and μRXS.

The quasimolecular theory in its simplest original version by Emelyanenko and Osipov [27] predicts the emergence of $\frac{1}{9}$, $\frac{1}{7}$, $\frac{1}{5}$, and $\frac{1}{4}$ between Sm-C_A^* and $\frac{1}{3}$. Naturally, $\frac{1}{8}$ and $\frac{1}{6}$ do not emerge, for their unit cells have sixteen and twelve layers, respectively, and the numerical calculations are restricted up to nine smectic layers. They further studied the influence of the long-range interaction due to polarization fluctuations and found that the most stable subphase other than $\frac{1}{3}$ and $\frac{1}{2}$ is $\frac{1}{4}$ [28]. The calculated unit cell has a microscopic highly distorted helical structure with a short pitch of $p_{qT} = 8/3$; the structure is almost flat and the approximate Ising structure is $(FAAAFAAA)$, which is exactly the same as experimentally determined. In the original version, the frustration between Sm-C_A^* and Sm-C^* alone is taken into account and hence the tilt angle is considered to be large and constant, temperature independent, and spatially uniform. By taking into account the frustration among Sm-C_A^*, Sm-C^*, and Sm-A with the tilt angle θ temperature dependent but still spatially uniform, the phase emerging sequence of (1), (2), and (3) appears to be understandable [14,51], although no detailed systematic studies have been made yet. On the other hand, the phenomenological Landau theory by Dolganov *et al.* [29,30] also results in the emergence of

a similar $\frac{1}{4}$ subphase with the eight-layer unit cell of the approximate Ising ($FAAAFAAA$) structure between Sm-C_A^* and $\frac{1}{3}$.

Now we move on to the antiferroelectric $\frac{2}{5}$ and ferrielectric $\frac{3}{7}$ subphases between $\frac{1}{3}$ and $\frac{1}{2}$. Emelyanenko and Osipov [27] originally predicted the emergence of $\frac{3}{7}$ but not the emergence of $\frac{2}{5}$, for their unit cells have seven and ten layers, respectively, and the numerical calculations were restricted up to nine smectic layers. When the calculations are expanded to include ten smectic layers, both $\frac{2}{5}$ and $\frac{3}{7}$ appear naturally. The calculated unit cells have microscopic highly distorted helical structures with the short pitches of $p_{qT} = 10/3$ and $7/2$, respectively; they are almost flat and the approximate Ising structures are ferrielectric ten-layer ($FAFAFAAFAA$) and ferrielectric seven-layer ($FAAFAFA$) [50,52]. By taking into account the frustration among Sm-C_A^*, Sm-C^*, and Sm-A with the tilt angle θ temperature dependent but still spatially uniform, however, the calculated approximate Ising structure of $\frac{2}{5}$ becomes antiferroelectric ten-layer ($FAFAAFAFAA$) [51]. Thus the calculated unit cells of both $\frac{2}{5}$ and $\frac{3}{7}$ reproduce the experimentally determined ones. On the other hand, the phenomenological Landau theory by Dolganov *et al.* [29,30] also results in the emergence of similar $\frac{2}{5}$ and $\frac{3}{7}$ subphases with the ten-layer and seven-layer unit cells of the approximate Ising ($FAFAAFAFAA$) and ($FAAFAFA$) structures between $\frac{1}{3}$ and $\frac{1}{2}$.

In this way, both models can explain the emergence of $\frac{1}{4}$, $\frac{2}{5}$, and $\frac{3}{7}$ subphases in the designated narrow temperature ranges together with the approximate Ising structures of their unit cells. At the same time, we immediately notice at least two differences. One is whether the tilt angle θ_i depends on i within the unit cell or not. As is clearly shown in Figs. 4 and 8 of Ref. [29], in fact, the phenomenological Landau model predicts the approximate Ising unit cells of $\frac{1}{4}$, $\frac{2}{5}$, and $\frac{3}{7}$ where the tilt angle θ_i is spatially nonuniform. In the quasimolecular model by Emelyanenko and Osipov, on the other hand, the tilt angle θ_i is presupposed to be spatially uniform by neglecting the second flexoelectric effect and hence by considering that the total polarization of a smectic layer is always parallel to the layer plane. The other difference lies in the detailed structures of the microscopic highly distorted helices with the short pitches of $p_{qT} = 8/3$, $10/3$, and $7/2$ for $\frac{1}{4}$, $\frac{2}{5}$, and $\frac{3}{7}$, respectively. Actually, both models illustrated the microscopic highly distorted helix structures of $\frac{1}{4}$ as in Fig. 8(e) of Ref. [29] and in Fig. 3(c) of Ref. [27], which look quite different from each other. The microscopic highly distorted helix structures of $\frac{2}{5}$ and $\frac{3}{7}$ were not calculated in the quasimolecular model in its simplest original version but can be easily obtained in its expanded version [50,52], as illustrated in Fig. 14. Again there exists a crucial difference between Fig. 8(g) of Ref. [29] and Fig. 14(a) in the microscopic highly distorted helix structure of $\frac{2}{5}$; no illustration for $\frac{3}{7}$ has been given in the phenomenological Landau model [29,30].

The two theoretical models presuppose considerably different LRILIs. Emelyanenko and Osipov considered the effective LRILI based on the intriguing concept of the discrete flexoelectric effect. There are two flexoelectric terms in the free energy; only the first one was taken into account and the second

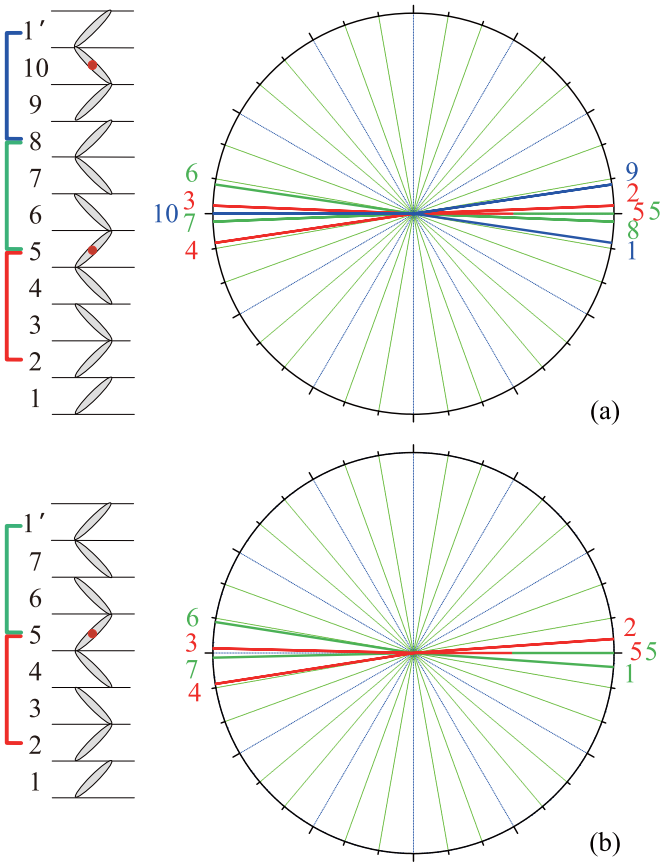

FIG. 14. Schematic illustrations of the microscopic highly distorted helical structures of (a) $\frac{2}{5}$ and (b) $\frac{3}{7}$ recalculated by the quasimolecular model with Ising unit cells consisting of up to ten smectic layers. The tilt directions in different layers are symmetrical with respect to the middle of the period, layers 5 and 10 in (a) and layer 5 in (b), indicated by closed red circles; this property defines the chirality of these subphases. We used the same parameter values as in Ref. [27]; the distortion angles do not change appreciably within the stable ranges of $\frac{2}{5}$ and $\frac{3}{7}$ illustrated in Fig. 12 of Ref. [50].

one was neglected on the assumption that the total polarization of a smectic layer may always be parallel to the layer plane. Therefore, in the quasimolecular model, the tilt angle is inevitably spatially uniform and the predicted unit cells of $\frac{1}{4}$, $\frac{2}{5}$, and $\frac{3}{7}$ have the microscopic highly distorted helix structures with constant tilt angles. The point is that, without considering spatially nonuniform tilt angles, the quasimolecular model can explain the experimentally observed emergence of $\frac{1}{4}$, $\frac{2}{5}$, and $\frac{3}{7}$ subphases in the designated narrow temperature ranges together with the approximate Ising structures of their unit cells. On the contrary, the phenomenological Landau model needs spatially nonuniform tilt angles; in fact, the predicted unit cells of $\frac{1}{4}$ and $\frac{2}{5}$ illustrate that θ_i depends on i. In this way, it is intriguing to ask which model describes the nature more appropriately and consider how to check this experimentally by studying the detailed subphase structures. Just observing the nonuniform tilt angle is not enough, for

the tilt angle θ_i may depend on i within the unit cell even in the quasimolecular model if the second flexoelectric term is taken into consideration; the appearance of the nonuniform tilt angle may be due to a secondary effect. We would like to perform polarized μRXS experiments to clarify the details of the microscopic highly distorted helix structures of suitable subphases in appropriate sample materials.

ACKNOWLEDGMENTS

This work was partly supported by Ireland-Japan cooperation and 13/US/I2866 Science Foundation Ireland grant as part of the USA-Ireland Research and Development Partnership program jointly administered with the United States National Science Foundation under Grant No. NSF-DMR-1410649. J.K.V. thanks the International Strategic Co-operation Award for cooperation between Ireland and Japan funded by the Science Foundation Of Ireland. The authors would like to thank Y. Ohtsuka and the staff of the Photon Factory for their help during the experiments. This work was carried out under the approval of the Photon Factory Advisory Committee (Proposals No. 2012G105 and No. 2014G154) and the Photon and Quantum Basic Research Coordinated Development Program. This work was partly supported by the Grant-In-Aid For Scientific Research On Priority Area (A) (Grant No. JP23246007) of the Ministry of Education, Culture, Sports, Science and Technology. This work was partially carried out the second hutch of SPring-8 BL03XU constructed by the Consortium of Advanced Softmaterial Beamline (FSBL), with Proposal No. 2015A7255.

[1] A. D. L. Chandani, E. Gorecka, Y. Ouchi, H. Takezoe, and A. Fukuda, Jpn. J. Appl. Phys. **28**, L1265 (1989).
[2] T. Isozaki, T. Fujikawa, H. Takezoe, A. Fukuda, T. Hagiwara, Y. Suzuki, and I. Kawamura, Phys. Rev. B **48**, 13439 (1993).
[3] A. Fukuda, Y. Takanishi, T. Isozaki, K. Ishikawa, and H. Takezoe, J. Mater. Chem. **4**, 997 (1994).
[4] P. Bak and R. Bruinsma, Phys. Rev. Lett. **49**, 249 (1982).
[5] R. Bruinsma and P. Bak, Phys. Rev. B **27**, 5824 (1983).
[6] P. Mach, R. Pindak, A.-M. Levelut, P. Barois, H. T. Nguyen, C. C. Huang, and L. Furenlid, Phys. Rev. Lett. **81**, 1015 (1998).
[7] P. Mach, R. Pindak, A.-M. Levelut, P. Barois, H. T. Nguyen, H. Baltes, M. Hird, K. Toyne, A. Seed, J. W. Goodby, C. C. Huang, and L. Furenlid, Phys. Rev. E **60**, 6793 (1999).
[8] A.-M. Levelut and B. Pansu, Phys. Rev. E **60**, 6803 (1999).
[9] T. Akizuki, K. Miyachi, Y. Takanishi, K. Ishikawa, H. Takezoe, and A. Fukuda, Jpn. J. Appl. Phys. **38**, 4832 (1999).
[10] P. M. Johnson, D. A. Olson, S. Pankratz, T. Nguyen, J. Goodby, M. Hird, and C. C. Huang, Phys. Rev. Lett. **84**, 4870 (2000).
[11] A. Cady, J. A. Pitney, R. Pindak, L. S. Matkin, S. J. Watson, H. F. Gleeson, P. Cluzeau, P. Barois, A.-M. Levelut, W. Caliebe, J. W. Goodby, M. Hird, and C. C. Huang, Phys. Rev. E **64**, 050702(R) (2001).
[12] I. Musevic and M. Skarabot, Phys. Rev. E **64**, 051706 (2001).
[13] V. P. Panov, N. M. Shtykov, A. Fukuda, J. K. Vij, Y. Suzuki, R. A. Lewis, M. Hird, and J. W. Goodby, Phys. Rev. E **69**, 060701(R) (2004).
[14] N. M. Shtykov, A. D. L. Chandani, A. V. Emelyanenko, A. Fukuda, and J. K. Vij, Phys. Rev. E **71**, 021711 (2005).
[15] A. D. L. Chandani, N. M. Shtykov, V. P. Panov, A. V. Emelyanenko, A. Fukuda, and J. K. Vij, Phys. Rev. E **72**, 041705 (2005).
[16] N. W. Roberts, S. Jaradat, L. S. Hirst, M. S. Thurlow, Y. Wang, S. T. Wang, Z. Q. Liu, C. C. Huang, J. Bai, R. Pindak, and H. F. Gleeson, Europhys. Lett. **72**, 976 (2005).
[17] P. Fernandes, P. Barois, E. Grelet, F. Nallet, J. W. Goodby, M. Hird, and J.-S. Micha, Eur. Phys. J. E **20**, 81 (2006).
[18] V. P. Panov, J. K. Vij, Y. P. Panarin, C. Blanc, V. Lorman, and J. W. Goodby, Phys. Rev. E **75**, 042701 (2007).
[19] K. L. Sandhya, J. K. Vij, A. Fukuda, and A. V. Emelyanenko, Liq. Cryst. **36**, 1101 (2009).
[20] K. L. Sandhya, A. Fukuda, and J. K. Vij, Mol. Cryst. Liq. Cryst. **511**, 36/[1506] (2009).
[21] S. Wang, L. D. Pan, R. Pindak, Z. Q. Liu, H. T. Nguyen, and C. C. Huang, Phys. Rev. Lett. **104**, 027801 (2010).
[22] J. Prost and R. Bruinsma, Ferroelectrics **148**, 25 (1993).
[23] R. Bruinsma and J. Prost, J. Phys. (France) **4**, 1209 (1994).
[24] M. B. Hamaneh and P. L. Taylor, Phys. Rev. Lett. **93**, 167801 (2004).
[25] M. B. Hamaneh and P. L. Taylor, Phys. Rev. E **72**, 021706 (2005).
[26] M. B. Hamaneh and P. L. Taylor, Phys. Rev. E **75**, 011703 (2007).
[27] A. V. Emelyanenko and M. A. Osipov, Phys. Rev. E **68**, 051703 (2003).
[28] A. V. Emelyanenko and M. A. Osipov, Ferroelectrics **309**, 13 (2004).
[29] P. V. Dolganov, V. M. Zhilin, V. K. Dolganov, and E. I. Kats, Phys. Rev. E **83**, 061705 (2011).
[30] P. V. Dolganov and E. I. Kats, Liq. Cryst. Rev. **1**, 127 (2014).
[31] Y. Takanishi, I. Nishiyama, J. Yamamoto, Y. Ohtsuka, and A. Iida, Phys. Rev. E **87**, 050503(R) (2013).
[32] C. C. Huang, S. Wang, L. Pan, Z. Q. Liu, B. K. McCoy, Y. Sasaki, K. Ema, P. Barois, and R. Pindak, Liq. Cryst. Rev. **3**, 58 (2015).
[33] Y. Takanishi, I. Nishiyama, and A. Iida, ILCC, Dublin, 2014 (unpublished).
[34] Y. Takanishi, A. D. L. Chandani, A. Fukuda, J. K. Vij, and A. Iida, ILCC, Kent, 2016 (unpublished).
[35] J. T. Mills, H. F. Gleeson, J. W. Goodby, M. Hird, A. Seed, and P. Styring, J. Mater. Chem. **8**, 2385 (1998).
[36] L. S. Hirst, S. J. Watson, H. F. Gleeson, P. Cluzeau, P. Barois, R. Pindak, J. Pitney, A. Cady, P. M. Johnson, C. C. Huang *et al.*, Phys. Rev. E **65**, 041705 (2002).
[37] L. S. Matkin, S. J. Watson, H. F. Gleeson, R. Pindak, J. Pitney, P. M. Johnson, C. C. Huang, P. Barois, A.-M. Levelut, G. Srajer, J. Pollmann, J. W. Goodby, and M. Hird, Phys. Rev. E **64**, 021705 (2001).
[38] T. Isozaki, Y. Suzuki, I. Kawamura, K. Mori, N. Yamamoto, Y. Yamada, H. Orihara, and Y. Ishibashi, Jpn. J. Appl. Phys. **30**, L1573 (1991).
[39] Y. Takanishi, Y. Ohtsuka, Y. Takahashi, and A. Iida, Phys. Rev. E **81**, 011701 (2010).
[40] A. Iida, I. Nishiyama, and Y. Takanishi, Phys. Rev. E **89**, 032503 (2014).

[41] A. Iida, Y. Takanishi, A. Fukuda, and J. K. Vij, Phys. Rev. E **94**, 052703 (2016).
[42] M. A. Osipov and M. V. Gorkunov, Liq. Cryst. **33**, 1133 (2006).
[43] M. Johno, K. Itoh, J. Lee, Y. Ouchi, H. Takezoe, A. Fukuda, and T. Kitazume, Jpn. J. Appl. Phys. **29**, L107 (1990).
[44] K. Hiraoka, H. Takezoe, and A. Fukuda, Ferroelectrics **147**, 13 (1993).
[45] J.-K. Song, A. Fukuda, and J. K. Vij, Appl. Phys. Lett. **93**, 142903 (2008).
[46] T. Qian and P. L. Taylor, Phys. Rev. E **60**, 2978 (1999).
[47] L. A. Parry-Jones and S. J. Elston, Phys. Rev. E **63**, 050701(R) (2001).
[48] L. A. Parry-Jones and S. J. Elston, Appl. Phys. Lett. **79**, 2097 (2001).
[49] A. D. L. Chandani, A. Fukuda, J. K. Vij, Y. Takanishi, and A. Iida, Phys. Rev. E **93**, 042707 (2016).
[50] A. Fukuda, Mol. Cryst. Liq. Cryst. **610**, 1 (2015).
[51] A. V. Emelyanenko and K. Ishikawa, Soft Matter **9**, 3497 (2013).
[52] K. L. Sandhya, A. D. L. Chandani, A. Fukuda, J. K. Vij, A. V. Emelyanenko, and K. Ishikawa, Phys. Rev. E **87**, 012502 (2013).